Effects of post-draw processing on the structure and functional properties of electrospun PVDF-HFP nanofibers

Adriano A. Conte[a], Khosro Shirvani[b], Harrison Hones[b], Alexander Wildgoose[b], Ye Xue[a], Raghid Najjar[b], Xiao Hu[a,c], Wei Xue[b], Vince Z. Beachley[a,*]

[a] Department of Biomedical Engineering, Rowan University, 201 Mullica Hill Road Glassboro, New Jersey, 08028, USA
[b] Department of Mechanical Engineering, Rowan University, 201 Mullica Hill Road Glassboro, New Jersey, 08028, USA
[c] Department of Physics and Astronomy, Rowan University, 201 Mullica Hill Road Glassboro, New Jersey, 08028, USA

HIGHLIGHTS

- Electrospun PVDF-HFP nanofibers were individually post-drawn by the thousands utilizing a parallel automated track device.
- Yield strength, Young's modulus, ultimate tensile strength, and voltage output were all enhanced with increasing draw ratio.
- The voltage output of PVDF-HFP nanofibers post drawn by 300% increased by four times in comparison to the undrawn control.
- Post-drawing increased polymer chain and crystal alignment, resulting in enhanced voltage output of PVDF-HFP nanofibers.

ARTICLE INFO

ABSTRACT

This study reports the effects of post-draw processing on the structural and functional properties of electrospun poly(vinylidene fluoride-co-hexafluoropropylene) (PVDF-HFP) nanofibers. Previous studies have independently demonstrated the potential of the electrospinning process or the post-drawing process to enhance the piezo-electric properties of PVDF nanofiber, and thin film structures respectively. However, post drawing electrospun nanofibers has been difficult to achieve. To overcome this limitation, a parallel automated track device was implemented to post-draw thousands of individual PVDF-HFP electrospun nanofibers per minute. Relationships were established showing that yield strength, Young's modulus, and piezoelectric output were enhanced with increasing draw ratio. The normalized voltage output of PVDF-HFP nanofibers post-drawn to a draw ratio of 3 increased by four-fold compared to undrawn control. We hypothesize that polymer chain and crystal alignment in the direction of the fiber axis, which were increased by post drawing, resulted in enhanced voltage output of PVDF-HFP nanofibers under mechanical stimulation.

1. Introduction

The fiber fabrication process known as electrospinning can be employed for the production of fibers with diameters on the scale of micro to nanometers. Electrospun fibers have demonstrated numerous useful characteristics among which are modifiable surface morphologies, increased surface area, and versatile surface functionality. Furthermore, possible applications of electrospun nanofibers include: tissue engineering, filtration, optoelectronics, sensors, wound healing, catalysis, textiles, drug delivery, and energy harvesting [1–7]. In electrospinning, electrostatic forces overpower the surface tension within a capillary needle, and subsequently pull a polymer droplet located in that needle into a Taylor cone. As the polymer is pulled from the capillary needle a

dynamic spiraling jet is ejected and collected. The unpredictable and forceful nature of the jet has been attributed to the instability of the fluid as well as that of the bending due to the electrostatic forces.

Typically, for various fiber fabrication techniques, there exists a relationship where reduction in fiber cross section results in significantly enhanced mechanical properties [8–10]. Specifically in electrospinning, as fiber diameters fall below 500 nm, there is a dramatic enhancement in mechanical strength [11–13]. Despite these findings, electrospun nanofibers are significantly weaker than much larger traditionally spun microfibers [14]. It is hypothesized that these disparities are due to a post drawing procedure present in the production process of traditional fibers that stretches the fiber to an extent that is many times its original length. This procedure is responsible for
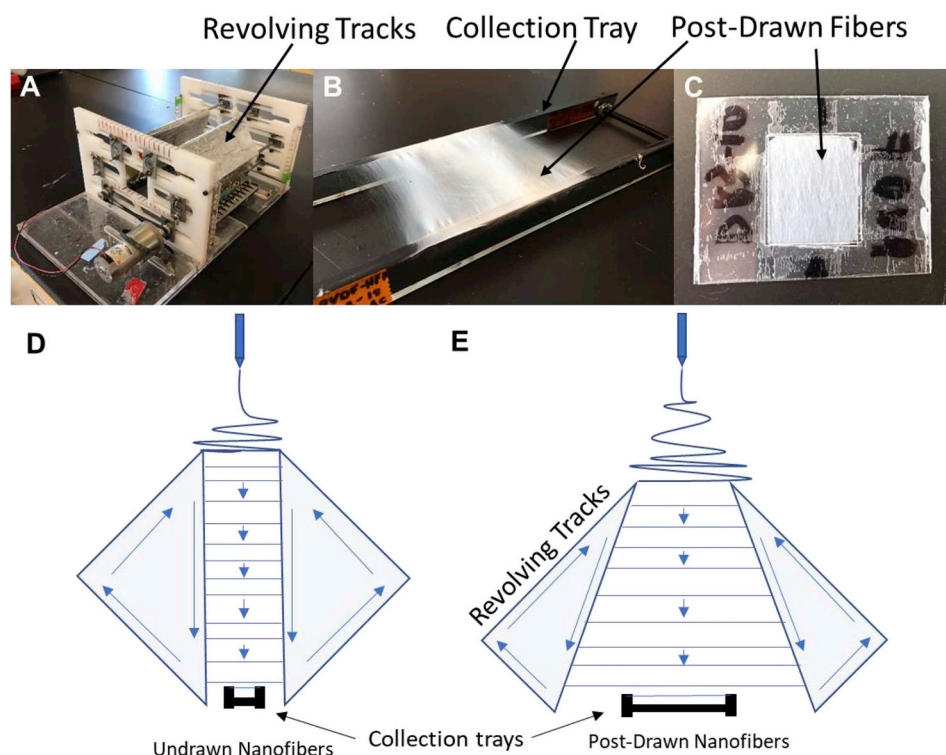
Fig. 1. (A) Variable draw ratio electrospinning system. **(B)** Collection tray containing electrospun PVDF-HFP nanofibers deposited from automated track system. **(C)** 10 mm by 10 mm window frame containing a sample of electrospun PVDF-HFP nanofibers. **(D)** Automated tracks enable continuous deposition of aligned individual fibers that are pulled down away from the initial collection area as they are deposited. **(E)** Modifiable angled tracks allow post-draw processing of thousands of individual fibers per minute as the fibers travel down the tracks to the final collection rack.

inducing macromolecular alignment within the fiber which in turn enhances mechanical strength. It can also be noted that post-drawing in the solid or semi-solid state prevents polymer relaxation that can quickly return the macromolecular structure to a highly disorganized state. In electrospinning the rapid elongations exerted on the polymer jet exiting the needle, but prior to collection, allow for a strain rate of $10^5 s^{-1}$ and a draw ratio of 10^5 [15,16]. Irrespective of these findings, electrospun nanofibers are molecularly disorganized with a common theory being fast chain relaxation occurring immediately after jet elongation. As a response to this dilemma, post drawing can be implemented in the electrospinning process utilizing a secondary collection stage where a semi-solid state fiber is produced as a result of unevaporated solvent in that fiber as a measure to prevent the polymer relaxation, thus improving the alignment and mechanical properties of electrospun fibers. A recent study facilitated an automated parallel track system as a both a collector and a means to successfully post draw thousands of aligned semi solid polycaprolactone (PCL) fibers individually [17]. In addition, this system has demonstrated the capacity to improve mechanical properties as well as macromolecular alignment of PCL nanofibers.

The electrospinable polymer, pure poly(vinylidene fluoride) (PVDF), exhibits piezoelectric properties and a high dielectric constant, which renders it suitable for energy transducers, sensors, and actuators [18–20]. The four crystalline formations of PVDF, α, β, γ, and δ, are determined by the chain conformation. The α-phase is the most widely accessible whereas the β-phase is the conformation responsible for PVDF's piezoelectric properties as a result of its highly polarized nature [21,22]. Various studies have examined how processing methods can increase the relative β-phase among crystalline formations and improve the electrical conversion efficiency of PVDF materials. The electrospinning process has resulted in enhanced electrical output of pure PVDF nanofibers [23–31] while the post-drawing of thin films has increased β-phase content [32–34]. The co-polymer poly(vinylidene fluoride-co-hexafluoropropylene) (PVDF-HFP) was chosen as a candidate for post-drawing due to the co-polymers superior mechanical strength to its pure PVDF counterpart [35,36]. Furthermore, PVDF-HFP has demonstrated low cost, advantageous ion conductivity, photo/

electrochemical stability and superior flexibility, which allows for easier processing [36–38]. Based on these findings, and this lab's unique ability to post-draw individual electrospun nanofibers, the aim of this study is to investigate the effects of the post-drawing process on the macromolecular alignment, mechanical properties, electroactive associated β-phase content, and electrical output of electrospun poly(vinylidene fluoride-co-hexafluoropropylene) (PVDF-HFP) nanofibers. The overall goal is to engineer electrospun PVDF nanofibers with enhanced energy harvesting piezoelectric capabilities.

2. Materials and methods

2.1. Electrospinning

1.5 g of the copolymer PVDF-HFP (pellets) at a molecular weight of 400,000 (Sigma-Aldrich) were dissolved in 4 mL of N,N-Dimethylacetamide (Sigma-Aldrich), and 2 mL of acetone (25% w/v) (Fisher Scientific). The solution was subsequently mixed on a heated shaker for 24 h at 65 °C to completely dissolve the PVDF-HFP pellets.

Electrospinning was carried out with a 7 kV applied voltage and a needle height, from the top of the automated tracks, of 10 cm for 20 min for all samples. A syringe pump (New Era Pump Systems) expelled the solution from the 21-gauge capillary needle at a set rate of 0.8 mL/h. Temperature was observed and ranged from 70 °F to 75 °F. The environment was controlled within an acrylic container housed in a fume hood. A humidifier (ReptiFogger; ZooMed) and a controller (HygroTherm; ZooMed) were connected to the container via plastic tubing, which allowed for a humidity inside the container of 50–70% which all samples were collected at [39].

2.2. Automated track system

An automated track system was employed as a collector for PVDF-HFP nanofibers for the purpose of post-drawing individual electrospun fibers prior to final collection onto a collection tray [17]. The system's track angles are adjustable for the function of lengthening fibers as they travel down these processing tracks. An acrylic material was

implemented to construct the walls, humidity container, and baseplate. A 12 V DC motor was employed to rotate the aluminum tracks. The tracks were fabricated using an inside layer of latex and an outside layer of aluminum foil tape. The automated parallel tracks were angled such that the length gap ratio between the top and the bottom of the tracks were 1:1, 1:2, and 1:3 respectively for each draw ratio ($DR = final\ fiber\ length/initial\ fiber\ length$) DR1/undrawn control, DR2 & DR3 respectively. The length gap ratio between the top and the bottom of the tracks were set as 1:1, 1:2, and 1:3 for top and bottom gaps of 4 cm–4 cm, 4 cm–8 cm, and 4 cm–12 cm respectively. The DR2 and DR3 conditions were implemented to examine the effects of post-drawing electrospun fibers by 200% (DR2) and 300% (DR3) in a semi-solid state prior to complete solvent evaporation and collection. Fig. 1 depicts the electrospinning apparatus and automated track system and describes the post-draw process of elongating fibers using angled parallel tracks. Six samples (n = 6) were collected for each condition which includes: draw ratio = 1 (DR1/undrawn control), draw ratio = 2 (DR2), and draw ratio = 3 (DR3). After collection, all samples were mounted to plastic frames measuring 10 mm by 10 mm, and set aside for characterization.

2.3. Fourier transform infrared (FTIR) spectroscopy

A Thermo Nicolet Nexus 670 FTIR was used to obtain information on the chemical absorbances of the samples, which enabled the calculation of β-phase (non-polarized FTIR), and polymer chain alignment (polarized FTIR). The spectra were taken with polarized light in the parallel and perpendicular directions in relation to the direction in which the fibers were post-drawn. A baseline was taken using the peak height tool for both absorbance and wavelength utilizing the FTIR software OMNIC. The spectra were observed in the 400 to 4000 cm^{-1} region. Characteristic peaks associated with the α-phase of PVDF were examined at 613 cm^{-1}, 761 cm^{-1}, and 1189 cm^{-1} [40,41], whereas characteristic absorption peaks for β-phase were examined at 490 cm^{-1}, 841 cm^{-1}, 881 cm^{-1}, 1072 cm^{-1}, 1280 cm^{-1}, and 1400 cm^{-1} [40–42]. The α-phase peak 761 cm^{-1} was specifically analyzed, using the Lambert-Beer law equation below, while the β-phase was assessed using the band at 841 cm^{-1}. Polymer chain alignment was assessed from the polarized FTIR data using the dichroic ratio equation (1) presented below [43]. The "A" in both of the following equations are representative of absorbance, and were ascertained directly from the peak height of interest utilizing the peak height tool in OMNIC.

$$DR = \frac{A_\perp - A_\parallel}{A_\perp + A_\parallel} \tag{1}$$

The piezoelectric associated β-phase content was calculated from the Lambert-Beer law with the following equation [32,44,46] (2):

$$F(\beta) = \frac{X_\beta}{X_\alpha + X_\beta} = \frac{A_\beta}{(1.26)A_\alpha + A_\beta} \tag{2}$$

X_α and X_β represent the crystal mass fraction of the α and β phase, whereas A_α and A_β are absorbances of α and β phase at 761 cm^{-1} and 840 cm^{-1} respectively.

2.4. X-ray diffraction (XRD)

PVDF-HFP samples of the film, undrawn, and draw ratio 3 groups were placed in a PANalytical Empyrean X-Ray diffractometer using Ni-filtered Cu Kα at a wavelength of 1.54 Å to ascertain crystalline data through x-ray diffraction (XRD). XRD recordings were observed over the range of 10°–70° 2Θ at 40 kV and 30 mA, with a scan duration of 0.056° per second and a step size of 0.013°. The software X'Pert Highscore Plus was then used to both baseline and smooth the data to be visually presented and analyzed.

2.5. Scanning electron microscopy imaging and analysis

Fiber diameter and fiber density were obtained using a desktop scanning electron microscope (SEM, Phenom Pure) where five images were taken at each of the magnifications which were 1,500x, 5,000x, and 10,000x. An ImageJ Cell Counter was utilized to count the number of fibers (using 1,500x images) within a 100-μm distance orthogonal to the direction in which the fibers were aligned. The measure tool in ImageJ was used to determine fiber diameters at a magnification of 10,000x. Both fiber diameter and fiber counts were averaged for each sample. Total number of fibers per sample was calculated by taking the number of fibers counted within the 100-μm distance, and that value was multiplied by 100 for the 10 mm window frame width.

2.6. Mechanical testing

Tensile testing was performed on a Shimadzu (model#: EZ-SX) mechanical tester for the purposes of ascertaining ultimate tensile strength and Young's modulus. A 2 N load cell was utilized in each of the tests. Tensile tests were executed at 5 mm/min until sample failure. The plastic frames previously assembled were loaded into the tensile test clamps, and the sides of the frames were cut so that the load was solely concentrated on the fibers and not the frame. Young's modulus was determined from the slope of the initial linear region of the stress-strain curve. The average cross-sectional area of each sample was calculated independently by multiplying the total number of fibers by the average individual fiber cross-sectional area $0.25 * \pi * (average\ fiber\ diameter)^2$ *(total # fibers in 10×10 mm sample). The stress was calculated by dividing the force values by the total cross-sectional area of a particular sample. The strain was determined from dividing the displacement values by the initial 10 mm window frame length. Yield Stress was determined by the inflection point at which the linear region of the stress strain curve terminates, and the nonlinear or plastic region begins.

2.7. PVDF electrical testing device and preparation

A two-part elastomer polydimethylsiloxane (PDMS) (Dow Corning) consisted of a base polymer and curing agent which were thoroughly mixed together at a ratio of 10 to 1 (25 g base polymer/2.5 g curing agent). Air bubbles were removed from the PDMS by placing the mix in a desiccator for 4 h. The resultant PDMS was then allowed to cure inside a petri dish for 24 h on a heated plate at 65 °C. The solidified PDMS was later removed from the petri dish, and carefully cut into 4 cm by 1.5 cm pieces with a scalpel.

PDMS was used as a substrate for electrical testing for the PVDF nanofibers. PDMS pieces previously mentioned were adhered with 4 double sided copper strips with dimensions of 6 mm by 2 ½ cm. Theses strips were adhered orthogonally to the long axis of the PDMS substrate and spaced 6 mm apart. A portion of the copper tape was wrapped around the other side of the PDMS substrate. Each subsequent copper strip adhered to the PDMS alternated in terms of which way the following strip wrapped around the underside of the PDMS. On the underside of the PDMS, 2 copper strips used as electrical leads measuring 6 mm by 5 cm were adhered parallel to the longer length of the PDMS substrate and on top of the orthogonal copper strip portions wrapped onto that side of the PDMS. The side of the PDMS with the orthogonally oriented copper strips was then adhered to the PVDF-HFP nanofibers on their collection tray in such a way that the fibers were parallel to the long axis of the PDMS substrate. The electrical device was then cut around using a razor blade to separate the electrical device from the rest of the fibers adhered to the collection tray. A thin 3 mm layer of uncured PDMS was then poured onto the fiber side of the PDMS device in such a way that the entire fiber surface was covered. This top layer was implemented for the purpose of completely encapsulating the underlying nanofibers while forming a bond with the pre-cured lower layer of
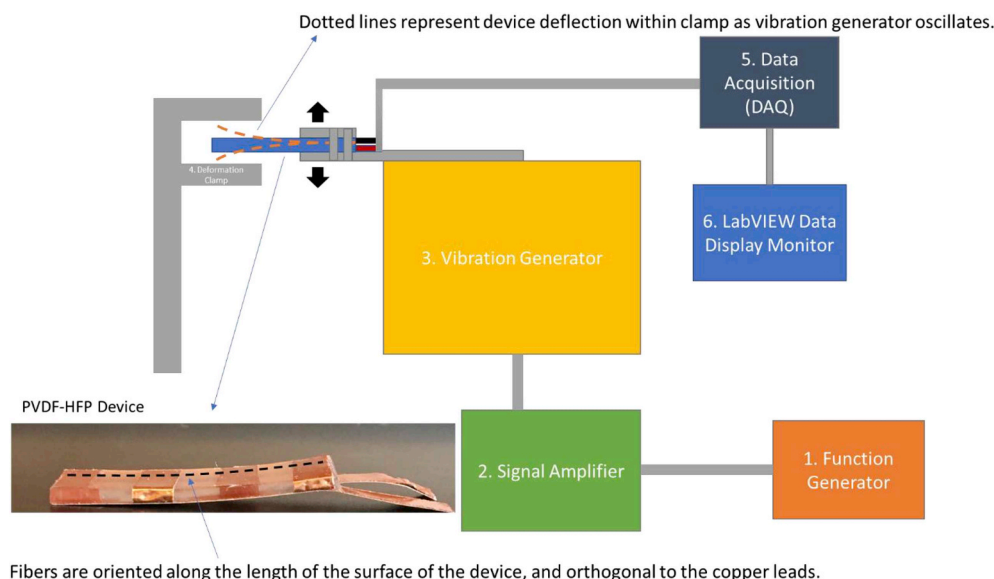
Dotted lines represent device deflection within clamp as vibration generator oscillates.

Fibers are oriented along the length of the surface of the device, and orthogonal to the copper leads.

Fig. 2. Mechanical-electrical measurement schematic for analyzing the PVDF-HFP electrical devices. DAQ stands for data acquisition system. A signal is produced by a function generator which is then amplified, and relayed to a vibration generator attached to the PVDF device. The device is then deflected in a deformation clamp. Copper leads attached to the PVDF nanofibers within the PDMS substrate deliver an electrical output to the DAQ which then sends this data to a computer monitor, and is displayed using LabVIEW as peak-to-peak voltage.
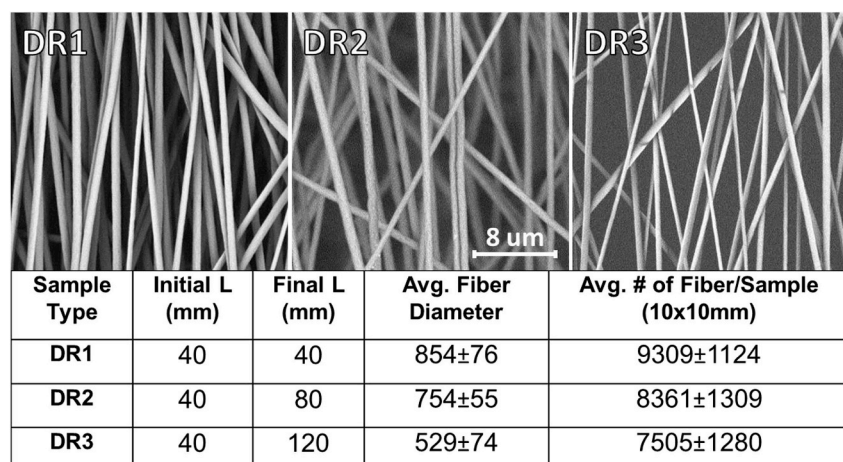

Fig. 3. (Top) Scanning electron microscope (SEM) images show PVDF-HFP nanofiber morphology for aligned samples collected with the automated track system (undrawn (DR1) to DR3). **(Bottom)** Average values of fiber diameters and total fiber # per sample (10×10 mm) are displayed with their standard deviation for n = 6 replicates for each group. All scale bars = 8 μm.

Sample Type	Initial L (mm)	Final L (mm)	Avg. Fiber Diameter	Avg. # of Fiber/Sample (10x10mm)
DR1	40	40	854±76	9309±1124
DR2	40	80	754±55	8361±1309
DR3	40	120	529±74	7505±1280

PDMS. For curing, the device was placed on a hot plate at 65 °C for 24 h.

2.8. Electrical testing system

A mechanical stimulation system was utilized to determine the energy output of the prepared PVDF-HFP devices associated with known mechanical deflections. The mechanical-electrical measurement system implemented is depicted in Fig. 2. A vibration was produced by a vibration device LW126 (Labworks Inc., Costa Mesa, CA, USA). A function generator BK Precision 4054 (B&K Precision Co., Yorba Linda, CA, USA) set to a frequency of 30 Hz provided a sinusoidal wave of an amplitude of 240 mV pp (peak-to-peak) to a linear power amplifier PA-141 (Labworks Inc., Costa Mesa, CA, USA) which amplified that signal, and relayed it to an electrodynamic magnet shaker ET-126B (Labworks Inc.). A rectangular acrylic plate was fastened to the top of the shaker. The PVDF-HFP device was fastened between the plate, and another much smaller orthogonal rectangular piece of acrylic plate at the end of the larger acrylic plate. The plane of the device was situated orthogonal to the shaker so that any vibrational force applied would also be orthogonal to the nanofiber plane. The PVDF-HFP device was made to protrude from the acrylic plates and magnetic shaker by about 2 cm. The protruding PVDF-HFP device was then inserted into a fixed clamp stand. The vibration generator then continuously oscillated the PVDF-HFP device within the fixed clamp in such a way that the device was perpetually being deformed by the fixed clamp itself. Electrical signals

were recorded by an oscilloscope BK Precision 2190D (B&K Precision Co.) in addition to a data acquisition device (DAQ) NI USB-4431 (National Instruments Co., Austin, TX, USA). LabVIEW software was utilized to collect the data for analyzing the electrical output of the PVDF-HFP devices associated with mechanical deformation. The peak-to-peak voltage output was measured and represented the mechanical to electrical translation performance of the PVDF-HFP devices. A sample size of three PVDF-HFP devices (n = 3) was used for each group for the electrical testing.

2.9. Statistical analysis

Overall group statistical analysis was performed using SPSS software for all diameter, mechanical, and electrical data using a Kruskall-Wallis-H test. Group to group statistical analysis was carried out using Welch's test on the same data.

3. Results

3.1. Nanofiber morphology and analysis

The SEM imaging in Fig. 3 of nanofibers collected with the automated track device (undrawn control (DR1), DR2, DR3) demonstrate an aligned orientation. All initial parallel track gaps were fixed at 40 mm with final gaps being situated at lengths appropriate to their intended
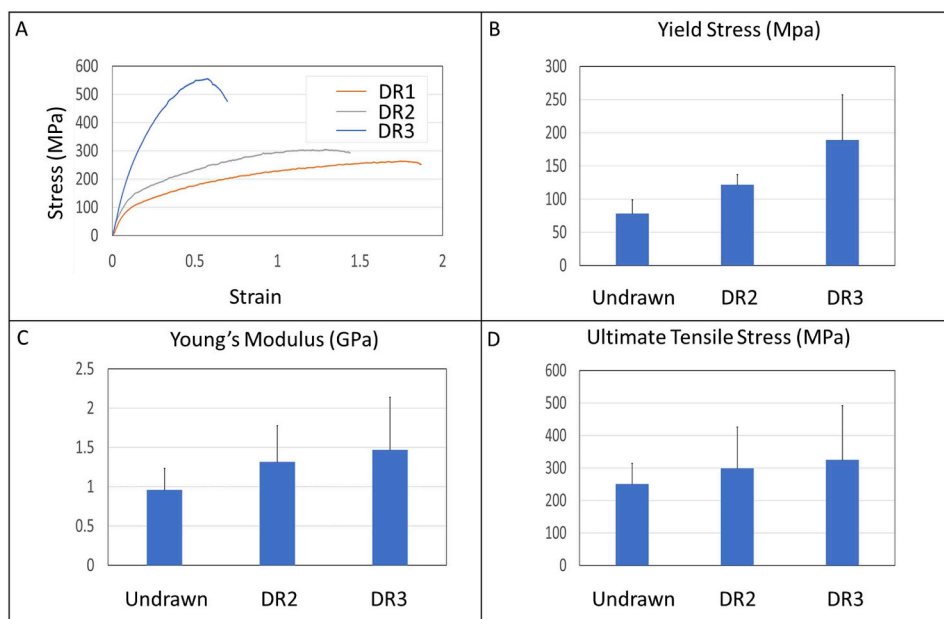
Fig. 4. (A) Stress-Strain curves from one sample each for undrawn control (DR1), DR2, DR3. Curves are cut off shortly after the ultimate tensile strength peak for visual presentability. **(B)** There is an increasing PVDF nanofiber yield stress from the undrawn control to DR3 (p < 0.01). **(C)** The Young's Moduli recorded showed continuous increases from undrawn (DR1) fibers through DR3. **(D)** Ultimate tensile strength also shows increases from undrawn fibers to DR3. (n = 6) for graphs (B–D).

draw ratio (DR1 = 40 mm, DR2 = 80 mm, DR3 = 120 mm). There was a statistically significant diameter reduction between draw ratios (p < 0.01). This diameter reduction is a result of fiber thinning with increasing elongation that would be expected assuming a similar total pre and post-drawn fiber volume. It was observed that from the undrawn nanofibers (DR1) to DR3 there was a reduction in fiber density (# of fibers per sample) but this change was not statistically different between draw ratios.

3.2. Mechanical testing

The representative stress strain curves depicted in Fig. 4A demonstrate an elevated tensile strength with increasing draw ratio with respect to the control undrawn nanofibers (DR1). There was an overall reduction in the strain occurring at the point of ultimate tensile stress from the undrawn control at a value of 1.48 to 1.24 at DR2 to finally 0.63 at DR3. Fig. 4B shows an overall increase in PVDF-HFP nanofiber yield stress by 141% from undrawn nanofibers at 78.35 MPa to 189.08 MPa in DR3 (p < 0.01). Fig. 4C presents a systematic increase in Young's modulus values from the undrawn control (DR1) through each subsequent draw ratio. In comparing DR1 (0.96 GPa) to DR3 (1.47 GPa) there is a 53% increase in Young's modulus. As shown in Fig. 4D, ultimate tensile strength (UTS) values show increases, particularly comparing DR1 (250.65 MPa) to DR3 (325.05 MPa) which amounts to a 30% increase.

3.3. FTIR analysis

It can be observed in Fig. 5A that alpha peaks at $761 \, cm^{-1}$ and $613 \, cm^{-1}$, which were present in film, almost completely disappear in the electrospun groups. The most prominent peaks observed in electrospun samples and analyzed in polarized FTIR were the bands at $1400 \, cm^{-1}$, $1278 \, cm^{-1}$, $1180 \, cm^{-1}$, $1070 \, cm^{-1}$, $881 \, cm^{-1}$, $840 \, cm^{-1}$, and $474 \, cm^{-1}$. The polarized FTIR data shown in Fig. 5C–E demonstrates that in all the PVDF-HFP samples there can be observed a relative intensity difference among the parallel and perpendicular spectras which is indicative of molecular order in the PVDF-HFP nanofibers.

There was a substantial increase in β-phase content from film to the undrawn control group (0.44–0.98). However, no net increase was observed from undrawn control to DR3 in β-phase content using the Beer-Lambert law (Equation (2)) with the β-phase peak selected at $840 \, cm^{-1}$ and α-phase at $761 \, cm^{-1}$ (Fig. 5F).

In reference to the polarized data displayed in Fig. 5G, dichroic ratio averages at bands $1278 \, cm^{-1}$, $840 \, cm^{-1}$, and $881 \, cm^{-1}$ exhibit polarized light absorbances higher when the infrared beam is oriented perpendicularly to the nanofiber axis. In contrast, the bands at $1400 \, cm^{-1}$, $1070 \, cm^{-1}$, $474 \, cm^{-1}$, and $1180 \, cm^{-1}$ have higher light absorbances when the beam is oriented parallel to the direction of the nanofibers. These observations are due to the bond angle relative to the polymer chain backbone as well as the conformation of the backbone within crystalline regions. For example, the peak at $1400 \, cm^{-1}$ showed a higher absorbance when the infrared beam was parallel to the fibers, and these bonds have been shown to align parallel to the PVDF backbone [43]. Where in comparison the $1280 \, cm^{-1}$ peak showed a higher absorbance when the beam was orthogonal to the fibers, and these bonds have been documented to align perpendicular to the PVDF backbone [43]. Post-drawing results in various chemical bonds (wavenumbers) to become more aligned parallel in relation to the fiber axis ($1400 \, cm^{-1}$ and $474 \, cm^{-1}$), whereas others become more aligned orthogonal to the fiber axis ($1278 \, cm^{-1}$, $881 \, cm^{-1}$, and $840 \, cm^{-1}$) with increasing draw ratio (Fig. 5G). A value of zero for dichroic ratio would be indicative of a disordered polymer chain. In terms of the orientation at which our samples were analyzed, a value closer to −1 is indicative of bonds or functional groups that are aligning parallel to the fiber axis. Values going to 1 are representative of bonds or functional groups that are aligning perpendicular to the fiber axis. Irrespective of specific bond orientation, increased absolute value of spectral differences observed in parallel versus perpendicular infrared absorbances are indicative of increasing molecular order with increasing draw ratio. In particular the band at $474 \, cm^{-1}$ displays a strong trend of increasing macromolecular alignment in the direction of the fiber axis with increasing draw ratio from a dichroic ratio of −0.250 in undrawn nanofibers to a dichroic ratio of −0.612 in nanofibers post drawn to DR3. Further analysis of this distinct wavelength revealed a significant change from PVDF film where the peak at $474 \, cm^{-1}$ does not occur and the closest peak is at $486 \, cm^{-1}$ (Fig. 5B).

3.4. XRD analysis

Fig. 6 presents an XRD film pattern containing two α-phase peaks at 17.7° and 19.9°, while not showing the presence of β associated peaks [44,45]. Both the undrawn and post-drawn DR3 groups show a relative shift in peaks with α associated peaks visible at 18.4° in addition to β-phase peaks at 20.3° [44,46–49]. The intense β related peaks in the
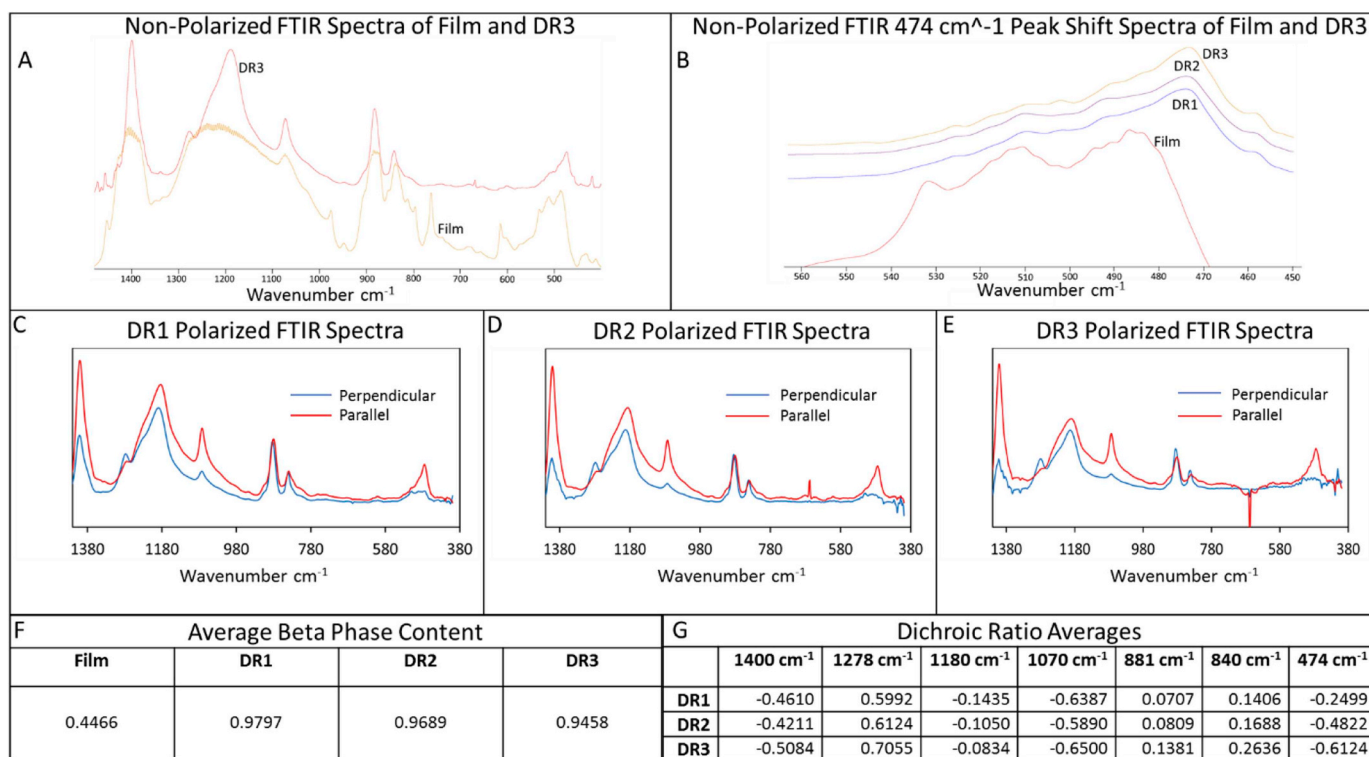
Fig. 5. (A) A Comparison of non-polarized FTIR spectras for the film and DR3 PVDF-HFP groups. The disappearance of the 613 cm^{-1} and 760 cm^{-1} bands indicate the α-β phase transformation from film to electrospun samples. **(B)** Non-polarized FTIR spectras for all groups at 474 cm^{-1}. **(C–E)** A comparison of the polarized FTIR spectra (400 cm^{-1} -4000cm^{-1}) of PVDF-HFP fiber samples for each condition (DR1, DR2, DR3). The characteristic absorption bands of β-phase at 474 cm^{-1}, 840 cm^{-1}, 881 cm^{-1}, 1070 cm^{-1}, 1278 cm^{-1}, and 1400 cm^{-1} are observed in all samples. **(F)** Average β-phase percentage for each group including film calculated using the Lambert-Beer law. **(G)** Dichroic ratio averages (n = 6) for the wavelengths located at 1400 cm^{-1}, 1278 cm^{-1}, 840 cm^{-1}, 1070 cm^{-1}, 474 cm^{-1}, 1180 cm^{-1}, and 881 cm^{-1}. Values approaching 1 are indicative of bond(s)/functional groups aligned perpendicular to the fiber axis, whereas values approaching −1 are representative of chemical bond(s)/functional groups aligning parallel to the fiber axis. A value of 0 is representative of random order.

electrospun groups are consistent with the FTIR findings, wherein relatively high β-phase content (95–98%) was observed in all electrospun groups in comparison to the film group (45%).

3.5. Mechanical-electrical testing

Piezoelectric PVDF–HFP nanofiber devices under sinusoidal mechanical stimulation produced a sinusoidal positive to negative voltage output associated with nanofiber device bending in opposing arches. Average peak-to-peak output voltages shown in Fig. 7C display an increase from 0.42 V in undrawn nanofiber devices (DR1) to 0.53 V for DR2, and another increase to 0.56 V for the DR3 experimental group. The average number of total PVDF-HFP nanofibers across electrical devices for the undrawn control, DR2, and DR3 were 16,044 ± 926, 13,677 ± 2,005, and 11,108 ± 2173 respectively. The mechanical-electrical performance testing results demonstrate a voltage output on the order of magnitude of micro volts per fiber. Post drawing resulted in a 66% increase from undrawn control (DR1) to DR2 and another 32% increase from DR2 to DR3. The total electrical output per fiber increased by 120% from DR1 to DR3. The voltage output per cross sectional area (V/mm^2) also increases with increasing draw ratio (Fig. 7C), where DR2 exhibits an approximate 106% increase in volume normalized voltage output over DR1, and the V/mm^2 in DR3 is about 4 times greater than observed in DR1. The voltage per cross sectional area is statistically significant between groups (p < 0.05) for DR1 to DR2, and for DR1 to DR3.

4. Discussion

Post-drawing has been considered the single most essential processing step for producing macromolecular alignment and enhanced polymer fiber strength [14]. In the absence of this critical step, electrospun nanofibers have been shown to display disorganized chains in addition to diminished functional properties resulting from rapid polymer chain relaxation. Traditionally, reduced fiber cross sectional areas have resulted in enhanced strength, where in contrast electrospun nanofibers have been an exception to that common finding. The discrepancy between electrospun nanofibers and industrially produced larger fibers could be attributed to the post-drawing procedure performed in the conventional manufacturing process which is not present in electrospinning. The automated track system described in this study is currently the only means of post-drawing individual electrospun nanofibers immediately upon collection prior to solvent evaporation within a continuous manufacturing system.

Electrospun PVDF-HFP diameters reported in this study (529–854 nm) are in agreement with other studies where diameters were shown to be anywhere from 100 to 1400 nm [50–53]. With respect to mechanical properties, the UTS observed in the DR3 nanofiber group exceeded values reported for PVDF-HFP nanofibers electrospun onto a drum collector (5.53–7.27 MPa) by two orders of magnitude [54]. A different study utilizing parallel plates as a collector for pure PVDF reported UTS values (150 MPa for a nanofiber diameter of 400 nm) on the same order of magnitude as this study, but the DR3 group (325.05 MPa for a nanofiber diameter of 529 nm) in this study still exceeded the closest diameter-matched-UTS by two times [55]. In addition, the current study's Young's modulus in the DR3 (1.47 GPa) post drawn group exceeds the range of 0.008–1.00 GPa for studies using flat and parallel plates [51,55,56]. The elevated ultimate tensile strength and Young's moduli values for parallel plate electrospinning in comparison to the flat plate may be attributed to electrostatic induced
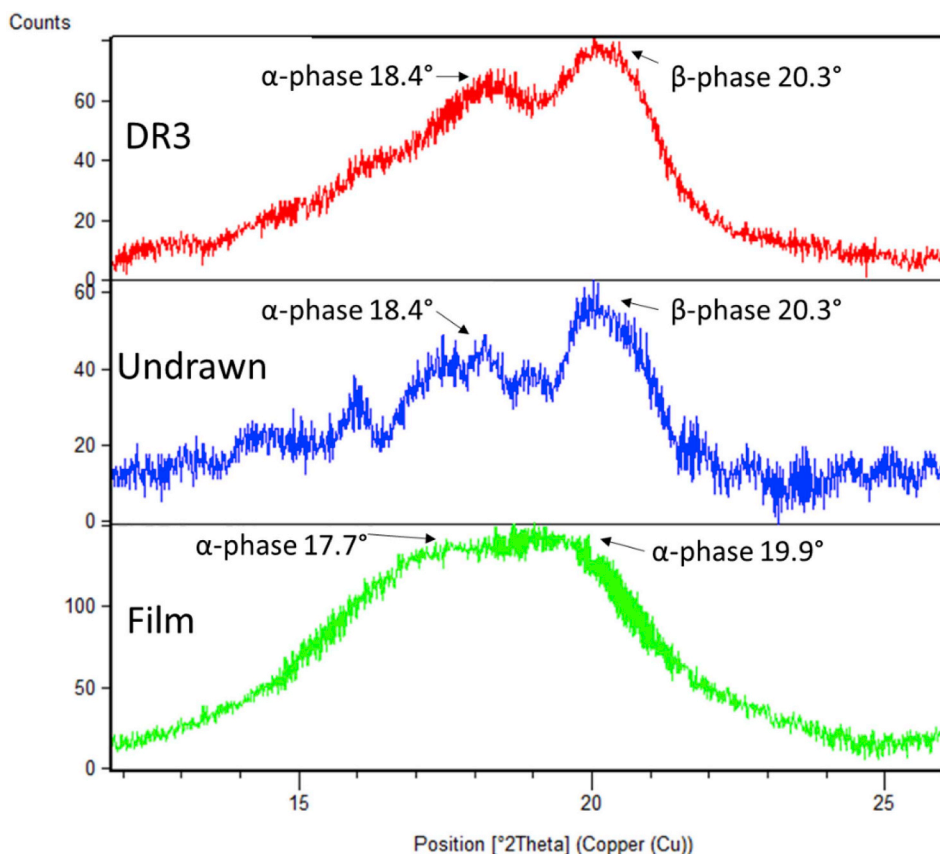
Fig. 6. XRD patterns of film (green color), undrawn nanofibers (blue), and draw ratio 3 (red). (For interpretation of the references to color in this figure legend, the reader is referred to the Web version of this article.)

extension of the polymer nanofiber across the parallel tracks just prior to collection, which is somewhat similar to the post-drawing just after collection investigated in this study. Furthermore, electrostatically induced extension of nanofibers collected across automated parallel

tracks has been shown to induce macromolecular alignment similar to post drawing results [43,57]. The previously mentioned studies indicate that polymer nanofibers electrospun onto a parallel plate collector may be several orders of magnitude stronger than those electrospun onto a
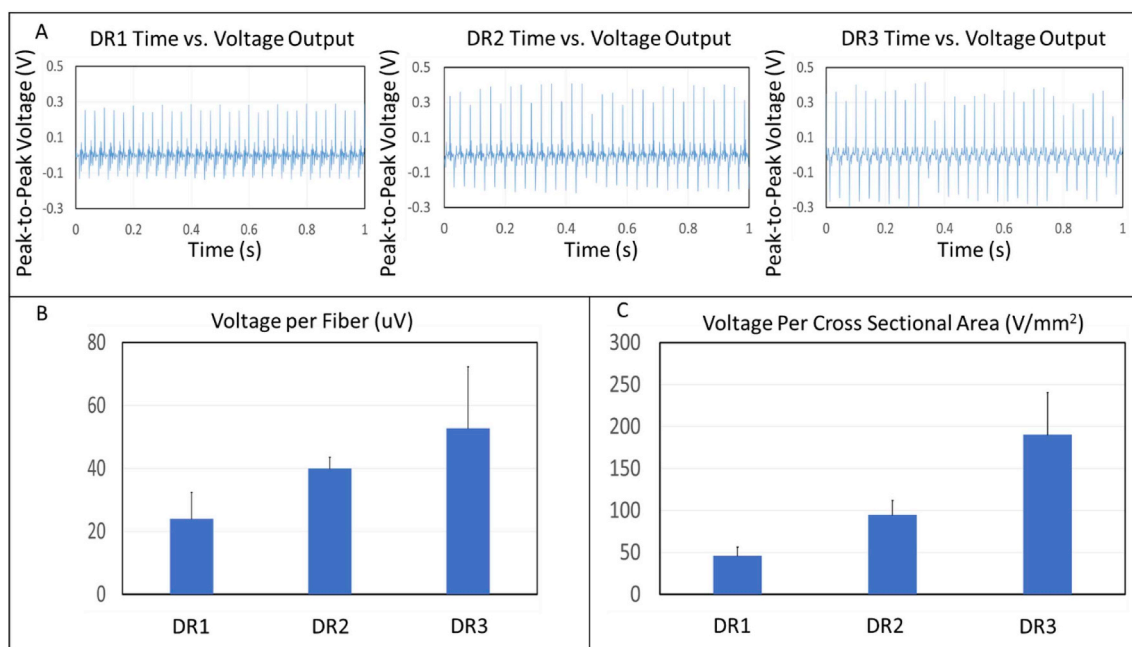

Fig. 7. (A) Peak to peak voltage outputs for undrawn fibers (DR1) in addition to the two post-drawn groups (DR2 & DR3). **(B)** Voltage generation per fiber shows an increasing trend with draw ratio. **(C)** Voltage per cross sectional area shows a statistically significant increase from DR1 to DR2, and from undrawn control (DR1) to DR3 (p < 0.05).

flat plate, and that post drawing further enhances these properties as a result of enhanced molecular order.

In relation to molecular vibrations associated with observed FTIR peaks, the peak located at $1180\,cm^{-1}$, representative of symmetric CF_2 stretching and the twisting of CH_2, is assigned to the α-phase [58,59]. The peak at $1400\,cm^{-1}$ (β-phase) is associated with both CH_2 wagging and CC antisymmetric stretching, and furthermore has an alteration in dipole moment parallel to the polymer backbone. The peak at $1280\,cm^{-1}$ (also β-phase) is related to symmetric stretching with respect to both CF_2 and CC, in addition to CCC bending. In contrast to the $1400\,cm^{-1}$ peak, the $1280\,cm^{-1}$ peak has its dipole moment altered orthogonally in relation to the polymer backbone. As the results have demonstrated, the bonds associated with the peak at $1400\,cm^{-1}$ become more aligned in a direction parallel to the fiber axis, while the bonds at the $1280\,cm^{-1}$ peak align perpendicularly with increasing draw ratios. This observation is indicative of the polymer backbone being directed in the same orientation as the fibers axis as a result of the post-drawing process [43]. Interestingly, the $474\,cm^{-1}$ peak, associated with the β-phase, demonstrated the largest dichroic ratio increases between draw ratios in comparison to all other peaks analyzed which may be of particular significance. This peak is less commonly discussed in the literature than many other β-phase peaks, and is not present in PVDF film. However, it is observed in other reports of electrospun PVDF, and appears to be the result of electrospinning in this study [40,42,59–61]. The previously noted studies associate the peaks at 473-475 cm^{-1} with the β-phase of PVDF. The $474\,cm^{-1}$ peak is also observed in another study where a supercritical PVDF solution was rapidly expanded through a heated capillary nozzle, which interestingly shares a high strain rate with the electrospinning process [62].

In reference to PVDF-HFP peak-to-peak electrical output, the results presented in the post-drawn groups are within range of the electrical generation of electrospun PVDF nanofiber devices in other studies reporting measurements between 0.005 V and 0.25 V [24,28,30,57]. Various devices and mechano-electrical designs play a role in overall device electrical output independent of the efficiency of the piezoelectric material being tested. Therefore, it's important to note that irrespective of the magnitude of voltage output, systematic increases in energy conversion were observed as draw ratios were increased. Since the total β-phase content did not appear to increase, the improved electrical performance of these devices with increasing draw ratio may be attributed to superior macromolecular and crystalline alignment experienced during post-drawn conditions which coincides with increases of total piezoelectricity of the post drawn samples. For example, the $474\,cm^{-1}$ peak associated with β-phase became much more aligned in the direction of the fiber axis with increased draw ratios. Increased electrical output may additionally be due to structural changes observed in the electrospun nanofibers such as the reported diameter reduction which also coincided with increasing draw ratio. In reference to scalability, the automated track collection system is a unique way to scale up parallel plate electrospinning. It allows for the continuous deposition of individual fibers while simultaneously preventing charge buildup and repulsion of fibers that would normally occur on a static parallel plate collector configuration. This collection system could be implemented in conjunction with various high throughput spinnerets for dramatically increased production rates of aligned nanofibers [63–66].

5. Conclusion

Post-draw processing of electrospun PVDF-HFP with an automated track collector for the first time has demonstrated the system's capability to engineer PVDF-HFP nanofibers with enhanced functional properties. Both mechanical and electrical property enhancement with increasing draw ratio may be ascribed to improved macromolecular and crystal alignment observed through polarized FTIR. We expect that post drawing PVDF nanofibers to higher draw ratios by optimizing

processing conditions such as temperature and draw rate would result in continued enhancement of both mechanical and piezoelectrical properties. Engineered PVDF nanofiber materials with enhanced piezoelectric responses and mechanical properties have the potential to impact society through many applications, such as high performance sensors, transducers, and energy harvesters.

Conflicts of interest

There are no conflicts of interest to declare.

References

[1] S. Agarwal, J.H. Wendorff, A.J.P. Greiner, Use of Electrospinning Technique for Biomedical Applications vol. 49, (2008), pp. 5603–5621.
[2] A. Greiner, J. Wendorff (Eds.), Self-Assembled Nanomaterials I, Springer, 2008, pp. 107–171.
[3] D. Li, Y. J. A. m. Xia, Electrospinning of nanofibers: reinventing the wheel? 16 (2004), pp. 1151–1170.
[4] D.J. Lipomi, Z.J.E. Bao, E. Science, Stretchable, Elastic Materials and Devices for Solar Energy Conversion vol. 4, (2011), pp. 3314–3328.
[5] X. Lu, W. Zhang, C. Wang, T.-C. Wen, Y.J.P.i.P.S. Wei, One-dimensional Conducting Polymer Nanocomposites: Synthesis, Properties and Applications vol. 36, (2011), pp. 671–712.
[6] D.H. Reneker, A.L.J.P. Yarin, Electrospinning jets and polymer nanofibers 49 (2008), pp. 2387–2425.
[7] J.D. Schiffman, C. L. J. P. r. Schauer, A Review: electrospinning of biopolymer nanofibers and their applications 48 (2008), pp. 317–352.
[8] S. Arbab, P. Noorpanah, N. Mohammadi, A.J.P.B. Zeinolebadi, Simultaneous Effects of Polymer Concentration, Jet-Stretching, and Hot-Drawing on Microstructural Development of Wet-Spun Poly (Acrylonitrile) Fibers vol. 66, (2011), pp. 1267–1280.
[9] A. Charuchinda, R. Molloy, J. Siripitayananon, N. Molloy, M. J. P. i. Sriyai, Factors Influencing the Small-Scale Melt Spinning of Poly (ε-Caprolactone) Monofilament Fibres vol. 52, (2003), pp. 1175–1181.
[10] E.J.C. Fitzer, Pan-based Carbon Fibers—Present State and Trend of the Technology from the Viewpoint of Possibilities and Limits to Influence and to Control the Fiber Properties by the Process Parameters vol. 27, (1989), pp. 621–645.
[11] Y. Ji, et al., Confinement-induced Super Strong PS/MWNT Composite Nanofibers vol. 84, (2008), p. 56002.
[12] C. Lim, E. Tan, S.J.A.P.L. Ng, Effects of Crystalline Morphology on the Tensile Properties of Electrospun Polymer Nanofibers vol. 92, (2008), p. 141908.
[13] D. Papkov, et al., Simultaneously Strong and Tough Ultrafine Continuous Nanofibers vol. 7, (2013), pp. 3324–3331.
[14] J. Yao, C.W. Bastiaansen, T.J.F. Peijs, High Strength and High Modulus Electrospun Nanofibers vol. 2, (2014), pp. 158–186.
[15] T. Kongkhlang, et al., Electrospun Polyoxymethylene: Spinning Conditions and its Consequent Nanoporous Nanofiber vol. 41, (2008), pp. 4746–4752.
[16] D.H. Reneker, A.L. Yarin, H. Fong, S. J. J. o. A. p. Koombhongse, Bending Instability of Electrically Charged Liquid Jets of Polymer Solutions in Electrospinning vol. 87, (2000), pp. 4531–4547.
[17] D.A. Brennan, et al., Concurrent Collection and Post-drawing of Individual Electrospun Polymer Nanofibers to Enhance Macromolecular Alignment and Mechanical Properties vol. 103, (2016), pp. 243–250.
[18] Q. Chen, P.J.M.S. Payne, Technology, Industrial applications of piezoelectric polymer transducers 6 (1995), p. 249.
[19] T. J. I. t. o. e. i. Furukawa, Piezoelectricity and Pyroelectricity in Polymers vol. 24, (1989), pp. 375–394.
[20] K. Koga, H. J. J. o. a. p. Ohigashi, Piezoelectricity and Related Properties of Vinylidene Fluoride and Trifluoroethylene Copolymers vol. 59, (1986), pp. 2142–2150.
[21] J. Chang, M. Dommer, C. Chang, L.J.N.E. Lin, Piezoelectric Nanofibers for Energy Scavenging Applications vol. 1, (2012), pp. 356–371.
[22] S.-H. Wang, Y. Wan, B. Sun, L.-Z. Liu, W. J. N. r. l. Xu, Mechanical and Electrical Properties of Electrospun PVDF/MWCNT Ultrafine Fibers Using Rotating Collector vol. 9, (2014), p. 522.
[23] C. Chang, V.H. Tran, J. Wang, Y.-K. Fuh, L. J. N. l. Lin, Direct-write Piezoelectric Polymeric Nanogenerator with High Energy Conversion Efficiency vol. 10, (2010), pp. 726–731.
[24] J. Chang, L. Lin (Eds.), Solid-state sensors, actuators and microsystems conference (TRANSDUCERS), IEEE, 2011, pp. 747–750 16th International.
[25] X. Chen, S. Xu, N. Yao, Y. J. N. l. Shi, 1.6 V Nanogenerator for Mechanical Energy Harvesting Using PZT Nanofibers vol. 10, (2010), pp. 2133–2137.
[26] X. Chen, S. Xu, N. Yao, W. Xu, Y. Shi, Potential Measurement from a Single Lead

Ziroconate Titanate Nanofiber Using a Nanomanipulator vol. 94, (2009), p. 253113, https://doi.org/10.1063/1.3157837.

[27] J. Fang, X. Wang, T.J.J.o.M.C. Lin, Electrical Power Generator from Randomly Oriented Electrospun Poly (Vinylidene Fluoride) Nanofibre Membranes vol. 21, (2011), pp. 11088–11091.

[28] B.J. Hansen, Y. Liu, R. Yang, Z. L. J. A. n. Wang, Hybrid Nanogenerator for Concurrently Harvesting Biomechanical and Biochemical Energy vol. 4, (2010), pp. 3647–3652.

[29] L. Li, M. Zhang, M. Rong, W.J.R.A. Ruan, Studies on the Transformation Process of PVDF from α to β Phase by Stretching vol. 4, (2014), pp. 3938–3943.

[30] D. Mandal, S. Yoon, K.J. Kim, Origin of Piezoelectricity in an Electrospun Poly (vinylidene Fluoride-Trifluoroethylene) Nanofiber Web-Based Nanogenerator and Nano-Pressure Sensor vol. 32, (2011), pp. 831–837, https://doi.org/10.1002/marc.201100040.

[31] G. Zhang, S. Xu, Y.J.M. Shi, N. Letters, Electromechanical Coupling of Lead Zirconate Titanate Nanofibres vol. 6, (2011), pp. 59–61.

[32] B. Mohammadi, A.A. Yousefi, S. M. J. P. t. Bellah, Effect of Tensile Strain Rate and Elongation on Crystalline Structure and Piezoelectric Properties of PVDF Thin Films vol. 26, (2007), pp. 42–50.

[33] A. Salimi, A.J.P.T. Yousefi, Analysis Method: FTIR Studies of β-phase Crystal Formation in Stretched PVDF Films vol. 22, (2003), pp. 699–704.

[34] A. Shirinov, W.J.S. Schomburg, A.A. Physical, Pressure Sensor from a PVDF Film vol. 142, (2008), pp. 48–55.

[35] L. Shi, et al., Fabrication of Poly (Vinylidene fluoride-co-hexafluoropropylene) (PVDF-HFP) Asymmetric Microporous Hollow Fiber Membranes vol. 305, (2007), pp. 215–225.

[36] A.K. Solarajan, V. Murugadoss, S.J.S.R. Angaiah, Dimensional Stability and Electrochemical Behaviour of ZrO 2 Incorporated Electrospun PVdF-HFP Based Nanocomposite Polymer Membrane Electrolyte for Li-Ion Capacitors vol. 7, (2017), p. 45390.

[37] K. Prabakaran, S. Mohanty, S.K. Nayak, PEO/PVdF–HFP Electrolytes for Natural Dye Sensitized Solar Cell Applications: Effect of Modified Nano-TiO 2 on Electrochemical and Photovoltaic Performance vol. 26, (2015), pp. 3887–3897.

[38] V. Elayappan, V. Murugadoss, S. Angaiah, Z. Fei, P.J. Dyson, Development of a Conjugated Polyaniline Incorporated Electrospun Poly (Vinylidene Fluoride-co-hexafluoropropylene) Composite Membrane Electrolyte for High Performance Dye-sensitized Solar Cells, (2015), p. 132.

[39] R.M. Nezarati, M.B. Eifert, E. Cosgriff-Hernandez, Effects of Humidity and Solution Viscosity on Electrospun Fiber Morphology vol. 19, (2013), pp. 810–819.

[40] X. Ma, et al., Molecular Orientation in Electrospun Poly (Vinylidene Fluoride) Fibers vol. 1, (2012), pp. 428–431.

[41] P. Martins, A. Lopes, S. J. P. i. p. s. Lanceros-Mendez, Electroactive phases of poly (vinylidene fluoride): determination, processing and applications 39 (2014) 683–706.

[42] T. Lei, et al., Electrospinning-induced Preferred Dipole Orientation in PVDF Fibers vol. 50, (2015), pp. 4342–4347.

[43] X. Ma, et al., The Effect of Collector Gap Width on the Extent of Molecular Orientation in Polymer Nanofibers vol. 54, (2016), pp. 617–623.

[44] L. Ruan, et al., Properties and Applications of the β Phase Poly (Vinylidene Fluoride) vol. 10, (2018), p. 228.

[45] K. Gao, X. Hu, C. Dai, T.J.M.S. Yi, E. B, Crystal Structures of Electrospun PVDF Membranes and its Separator Application for Rechargeable Lithium Metal Cells vol. 131, (2006), pp. 100–105.

[46] S.M. Damaraju, S. Wu, M. Jaffe, T.L.J.B.M. Arinzeh, Structural Changes in PVDF

[47] Fibers Due to Electrospinning and its Effect on Biological Function vol. 8, (2013), p. 045007.

[47] T. J. J. o. A. i. N. Zhang, Fabrication of Porous Structure of Electro-Spun PVDF Fibres vol. 3, (2018).

[48] A. Baji, Y.-W. Mai, Q. Li, Y.J.N. Liu, Electrospinning Induced Ferroelectricity in Poly (Vinylidene Fluoride) Fibers vol. 3, (2011), pp. 3068–3071.

[49] H. Shao, J. Fang, H. Wang, T. J. R. a. Lin, Effect of Electrospinning Parameters and Polymer Concentrations on Mechanical-To-Electrical Energy Conversion of Randomly-Oriented Electrospun Poly (Vinylidene Fluoride) Nanofiber Mats vol. 5, (2015), pp. 14345–14350.

[50] S.-S. Choi, et al., Electrospun PVDF Nanofiber Web as Polymer Electrolyte or Separator vol. 50, (2004), pp. 339–343.

[51] S.W. Choi, J.R. Kim, Y.R. Ahn, S.M. Jo, E. J. J. C. o. m. Cairns, Characterization of Electrospun PVDF Fiber-Based Polymer Electrolytes vol. 19, (2007), pp. 104–115.

[52] B.S. Lalia, E. Guillen-Burrieza, H.A. Arafat, R. J. J. o. m. s. Hashaikeh, Fabrication and Characterization of Polyvinylidenefluoride-Co-Hexafluoropropylene (PVDF-HFP) Electrospun Membranes for Direct Contact Membrane Distillation vol. 428, (2013), pp. 104–115.

[53] J.-Y. Park, et al., Dye-sensitized Solar Cells Based on Electrospun Poly (Vinylidenefluoride-co-hexafluoropropylene) Nanofibers vol. 70, (2013), pp. 507–515.

[54] C. Yao, X. Li, K. Neoh, Z. Shi, E.J.A.S.S. Kang, Antibacterial Activities of Surface Modified Electrospun Poly (Vinylidene fluoride-co-hexafluoropropylene)(PVDF-HFP) Fibrous Membranes vol. 255, (2009), pp. 3854–3858.

[55] A. Baji, Y.W. Mai, S.C.J.P.E. Wong, Science. effect of Fiber Size on Structural and Tensile Properties of Electrospun Polyvinylidene Fluoride Fibers vol. 55, (2015), pp. 1812–1817.

[56] G. Ico, et al., Size-dependent Piezoelectric and Mechanical Properties of Electrospun P (VDF-TrFE) Nanofibers for Enhanced Energy Harvesting vol. 4, (2016), pp. 2293–2304.

[57] V. Chaurey, et al., Interplay of Electrical Forces for Alignment of Sub-100 Nm Electrospun Nanofibers on Insulator Gap Collectors vol. 26, (2010), pp. 19022–19026.

[58] M. Bachmann, J.L. Koenig, Vibrational Analysis of Phase III of Poly (Vinylidene Fluoride) vol. 74, (1981), pp. 5896–5910.

[59] M. Kobayashi, K. Tashiro, H.J.M. Tadokoro, Molecular Vibrations of Three Crystal Forms of Poly (Vinylidene Fluoride) vol. 8, (1975), pp. 158–171.

[60] X. Cai, T. Lei, D. Sun, L.J.R.A. Lin, A Critical Analysis of the α, β and γ Phases in Poly (Vinylidene Fluoride) Using FTIR vol. 7, (2017), pp. 15382–15389.

[61] L. Yu, et al. (Ed.), 2013 13th IEEE International Conference on Nanotechnology, IEEE-NANO, 2013.

[62] S. Wolff, F. Jirasek, S. Beuermann, M.J.R.A. Türk, Crystal Phase Transformation of α into β Phase Poly (Vinylidene Fluoride) via Particle Formation Caused by Rapid Expansion of Supercritical Solutions vol. 5, (2015), pp. 66644–66649.

[63] Y.-K. Fuh, L.-C. Lien, S.-Y. Chen, Part B. High-Throughput Production of Nanofibrous Mats via a Porous Materials Electrospinning Process vol. 51, (2012), pp. 1742–1749.

[64] B. Lu, et al., Superhigh-throughput Needleless Electrospinning Using a Rotary Cone as Spinneret vol. 6, (2010), pp. 1612–1616.

[65] G. Jiang, S. Zhang, X.J.M.L. Qin, High Throughput of Quality Nanofibers via One Stepped Pyramid-Shaped Spinneret vol. 106, (2013), pp. 56–58.

[66] D. Wu, et al., High Throughput Tip-Less Electrospinning via a Circular Cylindrical Electrode vol. 10, (2010), pp. 4221–4226.